Bull Eng Geol Environ (2016) 75:1215–1225
DOI 10.1007/s10064-016-0906-2

ORIGINAL PAPER

Nonlinear dynamic simulation of offshore breakwater on sloping liquefied seabed

Jianhong Ye[1] · Duruo Huang[2] · Gang Wang[2]

Received: 16 November 2015 / Accepted: 26 May 2016 / Published online: 21 June 2016

Abstract Offshore structures are generally vulnerable to strong seismic waves propagating through a loose seabed foundation. However, only limited attention has been paid to the seismic stability of composite breakwaters. In this study, a coupled numerical analysis is performed to study the seismic dynamics of a composite breakwater on a sloping loose seabed foundation under a seismic wave recorded during the 2011 Tohoku earthquake ($M_L = 9.0$) in Japan. Computation results show that the developed numerical model is capable of capturing a variety of nonlinear phenomena in the interaction process between offshore structures and their loose seabed foundation. Under seismic loading, the loose seabed foundation away from the composite breakwater becomes completely liquefied. Because of the presence of the structure, the seabed foundation beneath the composite breakwater is partially liquefied. The composite breakwater undergoes significant subsidence, translation, and rotation; meanwhile, large lateral spreading occurs in the sloping seabed foundation. This investigation demonstrates that an advanced numerical method is promising in realistic evaluation of seismic performance of offshore structures.

Keywords Offshore breakwater · Seismic dynamics · Seabed foundation · Liquefaction · FSSI-CAS 2D

✉ Duruo Huang
drhuang@ust.hk

[1] State Key Laboratory of Geomechanics and Geotechnical Engineering, Institute of Rock and Soil Mechanics, Chinese Academy of Sciences, Wuhan 430071, Hubei, China

[2] Department of Civil and Environmental Engineering, Hong Kong University of Science and Technology, Clear Water Bay, Kowloon, Hong Kong

Introduction

In recent years, composite breakwaters are widely constructed to protect ports and harbors. The stability of these structures under environmental loading, including ocean waves and possible earthquakes, is the main concern in engineering design. Ocean waves are a conventional environmental loading for all offshore structures, the effect of which has been widely investigated on the stability of composite breakwaters (Ye 2012a). However, little attention has been paid to the seismic stability of this type of structure. In fact, it has been reported that a great number of offshore structures failed due to seabed liquefaction during significant earthquakes in the past (Sumer et al. 2007), such as the 1999 Kocaeli earthquake in Turkey ($M_L = 7.4$) and the 2003 Tokachi-oki earthquake in Japan ($M_L = 8.0$). Characteristics of soil liquefaction during major earthquakes have been extensively studied over the past decade using shaking table test, centrifuge modeling, and numerical simulation (e.g., Elgamal et al. 2005; El Shamy et al. 2010; Huang et al. 2008; Lu et al. 2011; Wang and Xie 2014; Xia et al. 2010; Ye et al. 2007). However, research on earthquake-induced liquefaction in the seabed foundation of offshore structures is still limited. In a few investigations, seismic dynamics of breakwaters have been analyzed using simple numerical models, as summarized by Ye (2012c). Most recently, Ye and Wang (2015, 2016) studied the liquefaction mechanism of a seabed in the offshore environment and complex seismic dynamics of offshore breakwaters on a liquefied seabed using advanced numerical modeling. These studies demonstrated the importance of using advanced numerical techniques in the study of these complicated phenomena.

In this study, the coupled numerical model FSSI-CAS 2D is used to investigate the seismic performance of a

composite breakwater on a sloping Quaternary seabed foundation, as the seabed floor is often gently sloping in offshore areas. Previous investigations usually assume the seabed is flat. Liquefaction and lateral spreading of soils in a sloping seabed are much more severe than those of a flat seabed. Computationally, it is more difficult to simulate a sloping seabed foundation than the flat case. An advanced soil constitutive model, the Pastor-Zienkiewics Mark III (PZIII) model (Pastor et al. 1990), is used to describe the complicated nonlinear dynamic behavior of the sloping Quaternary seabed. A seismic wave recorded off the Pacific coast during the 2011 Tohoku earthquake in Japan is adopted as the input excitation in the simulation. Computational results show that the coupled numerical model FSSI-CAS 2D is capable of capturing tilting, rotation of the composite breakwater, as well as large lateral spreading of the loose Quaternary seabed foundation under earthquake loading.

Coupled numerical model

In the offshore environment, offshore structures, seabed foundation, and sea water form a coupled system. There are three types of interactions among them: sea water–structures interaction, sea water–seabed interaction, and structures–seabed interaction, respectively. Previous investigations indicate that it is difficult to model effectively the porous seabed in the ocean wave–structures interaction analysis using traditional computational fluid dynamics; meanwhile, complex offshore structures cannot be accounted for in the investigation of ocean wave–seabed interaction. Regarding the issue of fluid–structure–seabed interaction (FSSI), a coupled numerical model FSSI-CAS 2D was recently developed by Ye (2012a) to overcome previous limitations, which uses the Volume Averaged/Reynolds Averaged Navier–Stokes (VARANS) equation (Hsu et al. 2002) to govern the wave motion and porous flow in the porous seabed, and the system is solved using the finite difference method; the dynamic Biot's equation, known as "*u–p*" approximation (Zienkiewicz et al. 1980), is adopted to describe the dynamic behavior of the offshore structure and its seabed foundation, which is solved in the finite element framework. A coupled algorithm is developed to integrate these two governing equations together, forming a coupled/integrated numerical model for the problem of fluid–seabed–structure interaction. More detailed information on solving the VARANS equation and the dynamic Biot's equation can be found in Ye (2012a), Ye et al. (2013) and Zienkiewicz et al. (1999). The developed coupled model FSSI-CAS 2D has been validated by analytical solutions, a series of wave flume tests, and a centrifuge test (Ye et al. 2013). It has been successfully applied to investigate the dynamics of breakwater and its seabed foundation to several types of ocean waves, such as regular waves, breaking waves, and tsunami waves.

Under earthquake loading, the variation of void ratio of the seabed soil needs to be updated in each computational step following Eq. (1):

$$e_{n+1} = (1 + e_n) \exp\left(\frac{\Delta p}{Q} + \Delta\varepsilon_{VS}\right) - 1 \tag{1}$$

where n represents the nth time step, Δp denotes the incremental pore pressure, and $\Delta\varepsilon_{VS}$ stands for the incremental volumetric strain of soils. Q is the compressibility of pore fluid. Correspondingly, permeability of the seabed soil k varies following $k = C_f \frac{e^3}{1+e}$, where C_f is an empirical coefficient determined by the initial void ratio e_0 and permeability k_0 via $C_f = k_0 \frac{1+e_0}{e_0^3}$. In addition, in order to handle large deformation of the seabed soil and offshore structures, the updated Lagrangian scheme is used in the finite element framework. The hydrostatic water pressure acting on interfaces between sea water, seabed, and offshore structures are also updated as boundary values in the finite element computation following the earthquake-induced deformation of the seabed foundation and the movement of offshore structures.

Newly deposited Quaternary sediments exist widely in the offshore environment, and a great number of offshore structures have been built on the sloping seabed in the engineering practice. Under earthquake loading, loose or medium dense Quaternary seabed soils are contractive due to rearrangement of soil particles. An elastoplastic soil model is needed to describe the dynamic behavior of Quaternary seabed soils. In FSSI-CAS 2D, the well-known Pastor-Zienkiewics-Mark III (PZIII) (Pastor et al. 1990; Zienkiewicz et al. 1999) is used. The reliability of PZIII has been extensively validated by a series of laboratory tests involving monotonic and cyclic loading (Zienkiewicz et al. 1999; Manzanal et al. 2011). This model was developed by Olek Zienkiewicz (Pastor et al. 2011).

Boundary conditions, input motion, and model parameters

The configuration and dimensions of the FEM computational domain are shown in Fig. 1. The composite breakwater consists mainly of a concrete caisson and a rubble mound, sitting on a sloping Quaternary seabed floor with a 2:100 gradient. The Quaternary seabed soil is modeled using PZIII, with model parameters listed in Table 1, which were calibrated by Zienkiewicz et al. (1999) in the VELACS project for Nevada sand (Dr = 60 %). We used these parameters in this study to present a typical seabed soil. For site specific analysis, a series of triaxial tests have to be conducted to determine these model parameters.

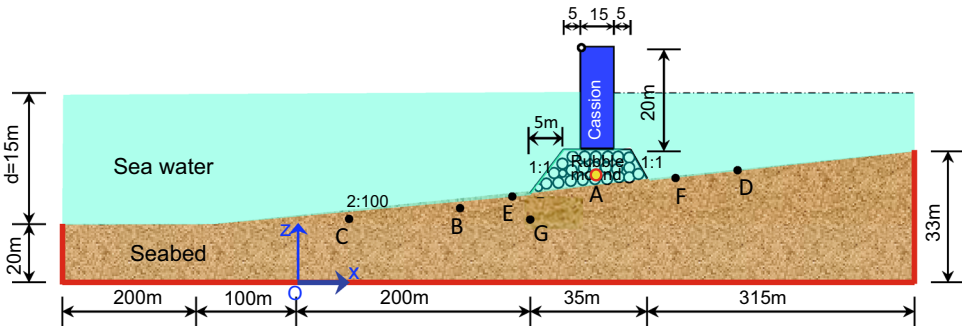

Fig. 1 Configuration and dimension of computational domain for the breakwater–seabed system (not to scale)

Table 1 PZIII model parameters of the seabed soil

K_{evo} (kPa)	G_{eso} (kPa)	p_0' (kPa)	M_g	M_f	α_f	α_g	β_0	β_1	H_0	H_{U0} (kPa)	γ_u	γ_{DM}
2000	2600	4	1.32	1.3	0.45	0.45	4.2	0.2	750	40,000	2.0	4.0

Table 2 Properties of the seabed soil, rubble mound and concrete caisson used in the simulation

Medium	E (N/m^2)	ν	k (m/s)	n	Sr
Seabed foundation	–	–	1×10^{-5}	0.4	0.98
Rubble mound	10^9	0.33	2×10^{-1}	0.35	0.99
Concrete caisson	10^{10}	0.25	0	0.1	0.95

Model properties of the breakwater system are listed in Table 2. The horizontal length of the computational domain is 850 m. The distances from the left and right lateral side to the composite breakwater are 315 and 500 m, respectively, which effectively eliminate the effect of the lateral boundary condition on the dynamic response of the seabed in the region near the composite breakwater. In computation, both the concrete caisson and the rubble mound are modeled as elastic materials. Because the rubble mound is made of concrete blocks and/or large gravels, its bearing capacity and stiffness are much higher than those of the seabed foundation. Shear deformation of the rubble mound is much less than that of the loose seabed foundation, so the irrecoverable plastic volumetric deformation in the rubble mound induced by earthquake loading can be generally ignored. Therefore, the elastic model is still acceptable because emphasis of the study is large deformation of the seabed foundation. In addition, the stiffness-proportional Rayleigh damping model is applied to stabilize the numerical results. $\alpha = 0$ and $\beta = 0.0003$ are used following Wang and Sitar (2011). In the computation, the following boundary conditions are applied:

1. The bottom of the seabed foundation is treated as a rigid and impermeable boundary;
2. Hydrostatic water pressure is applied perpendicularly on the surface of the seabed and the outer surface of the composite breakwater. The upward buoyant force of sea water is applied on the bottom of the caisson. The pore pressure is continuous at the interfaces between the seabed, breakwater, and sea water. In addition, the wave loading is not considered because it is a small probability event for a large ocean wave to occur simultaneously with a strong earthquake. It should be also noted that ripple wave resulted from the vibration of seabed and marine structures is usually negligible, so it is not considered in the current study.

   In this investigation, we found that large deformation occurs in the sloping seabed foundation close to the breakwater. As a result, the hydrostatic pressure acting on the breakwater and the seabed foundation changes significantly in the process of earthquake loading. To the best of the authors' knowledge, the numerical computation will be convergent only if the variation of hydrostatic pressure on the breakwater and its seabed foundation is updated following the deformation of seabed and breakwater. Therefore, in each time step, the hydrostatic pressure on breakwater and its seabed foundation is updated based on seabed deformation and breakwater movement.
3. The input seismic wave is applied on the two lateral sides and the bottom of computational domain simultaneously, making the boundary of the computational domain behave like a rigid container. Note that the lateral boundary is located 300–500 m away from the breakwater, so it will not significantly affect the behaviors of the breakwater and underlying seabed.

In this study, seismic waves recorded at station MYGH03 (141.6412E, 38.9178N) during the 2011 Tohoku earthquake ($M_L = 9.0$) are obtained from the KiK-net database operated by NIED, as shown in Fig. 2. The recording station is close to the Pacific coast so that the

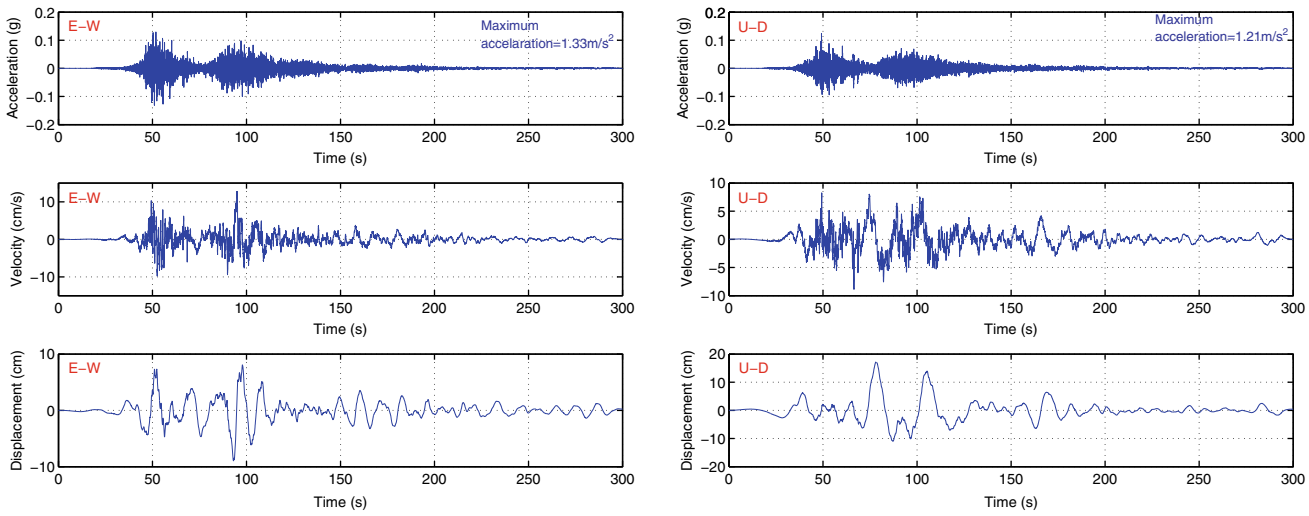

(a) E-W **(b)** U-D

Fig. 2 Input seismic wave recorded at the station MYGH03 during the 2011 M9.0 Tohoku earthquake in Japan

seismic waves adopted in this study are suitable representatives of earthquake waves in the offshore environment.

Seismic dynamics of composite breakwater

At first, the initial consolidation of the seabed–breakwater system under hydrostatic water pressure is determined before the input seismic wave is applied. More detailed analysis about the initial consolidation can be found in Ye (2012b) and Ye et al. (2012). With the initial condition specified, seismic dynamics of breakwater and its seabed foundation are determined numerically. In this study, a total of 9629 quad elements and 20,190 nodes are used to discretize the computational domain. The mesh size is 2 m in the x-direction, and 0.5–1 m in the z-direction. The time step size used in seismic analysis is 0.005 s, and the simulated shaking duration is 300 s.

In the offshore environment, breakwaters are easy to fail under strong earthquake shaking if they are built on Quaternary loose seabed floor. Therefore, seismic dynamics of a breakwater should be considered in the design practice in seismic active regions. The response acceleration and displacement of breakwaters are two key kinematic parameters required to be monitored. Figure 3 illustrates the response acceleration time history of the caisson at its top-left corner ($x = 210$ m, $z = 51$ m). It can be observed that the horizontal and vertical maximum acceleration are 1.99 and 1.42 m/s^2, respectively. There are two peak acceleration zones in both the horizontal and vertical directions, corresponding to the peak acceleration in the input seismic wave. Under the same input motion, the response acceleration of the same breakwater could be as large as 1 g if the foundation is made of a very dense soil based on a

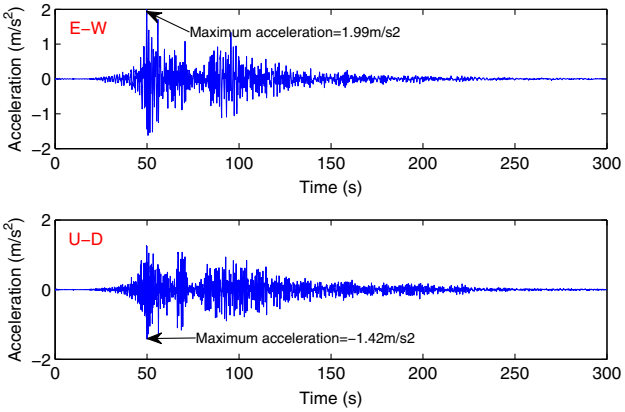

Fig. 3 Response acceleration time histories in EW and UD directions at the *top-left corner* ($x = 210$ m, $z = 51$ m) of the caisson

previous investigation by Ye (2012c), indicating that the loose seabed absorbs and damps a significant amount of seismic wave energy due to highly nonlinear and hysteretic behaviors of the loose seabed under cyclic loading. However, liquefaction and large deformation can occur in a less dense seabed, resulting in structure failure. It has been demonstrated that a dense seabed floor is much better compared to a loose one as a natural foundation for offshore structures (Sumer et al. 2007).

Figure 4 illustrates the displacement time history and rotation of the rigid caisson. It can be observed that the breakwater significantly subsided downward and moved to the left. The magnitude of subsidence reaches 5 m, and its top-left corner displaces 13 m to the left, accompanied by an anti-clockwise rotation of the caisson up to 17°. It can be also observed that the downward subsidence is the dominant motion of breakwater before $t = 100$ s. Afterwards, the

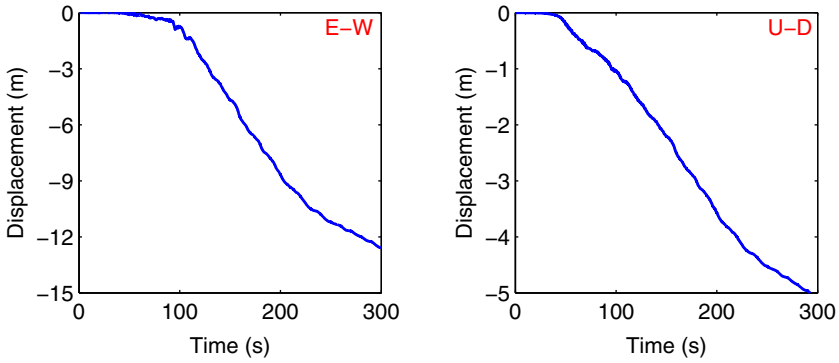

(a) Displacement at (x=210m, z=51m)

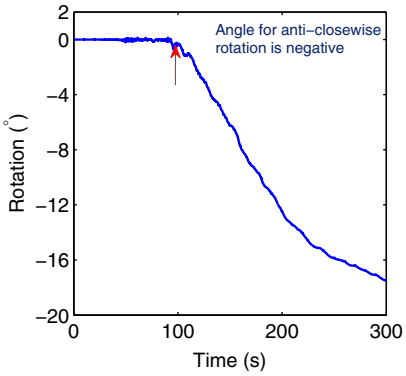

(b) Rotation of the caisson

Fig. 4 **a** Displacement time history at the *top-left corner* ($x = 210$ m, $z = 51$ m) of the caisson; **b** rotation of the caisson

horizontal displacement of breakwater increases quickly. As a result, the breakwater tilts to the left side. Based on the subsequent analysis, it can be concluded that the reason the breakwater quickly tilts to the left side is that part of the seabed foundation beneath the breakwater becomes liquefied and softens after $t = 100$ s under seismic loading.

In engineering practice, a rubble mound generally consists of large stones and/or gravels. In this seismic analysis, the rubble mound is treated as a permeable medium with large voids. The pore pressure and effective stress in this rubble mound are monitored in the computation. Figure 5 shows the time history of pore pressure and effective stress in the rubble mound at position A ($x = 217.5$ m, $z = 27.3$ m) shown in Fig. 1. It can be observed that the pore pressure in the rubble mound continuously increases. Actually, the increase in pore pressure is not due to the elasto-plastic deformation of the rubble mound, but due to the subsidence of the rubble mound under seismic loading. In the offshore environment, the static water level of sea water is virtually constant when the input seismic wave passes through the computational domain. As a result, the hydrostatic pore pressure at position A increases continuously with the earthquake-induced subsidence of breakwater. It is also interesting to observe that σ_z' increases continuously before $t = 100$ s. After that, σ_z' decreases. This phenomenon is attributed to the complex movement of the breakwater. As analyzed above, the breakwater tilts to left after $t = 100$ s. The tilting and rotation of the caisson make the gravity center of the caisson also move to the left side. As a result, the vertical effective stress σ_z' at A, which initially is under the gravity center of the caisson, decreases after $t = 100$ s. The shear stress at A also significantly increases after $t = 100$ s, with its peak approaching 330 kPa.

Seismic dynamics of seabed foundation

In this section, seismic dynamics and liquefaction potential of the seabed foundation are investigated. Figure 6 presents the acceleration response time history of the seabed foundation at position B ($x = 140$ m, $z = 23.8$ m) illustrated in Fig. 1, which is away from the composite breakwater. It can be observed that the maximum response accelerations in E–W and U–D at position B are 0.86 and 2.91 m/s^2, respectively. The maximum acceleration in E–W (0.86 m/s^2) is less than that of the input ground motion, due to the energy absorption of the seabed soil. Moreover, the response acceleration in E–W at the same position is greatly reduced after 60 s, which can be attributed to the liquefaction of seabed soil. After liquefaction, the seabed

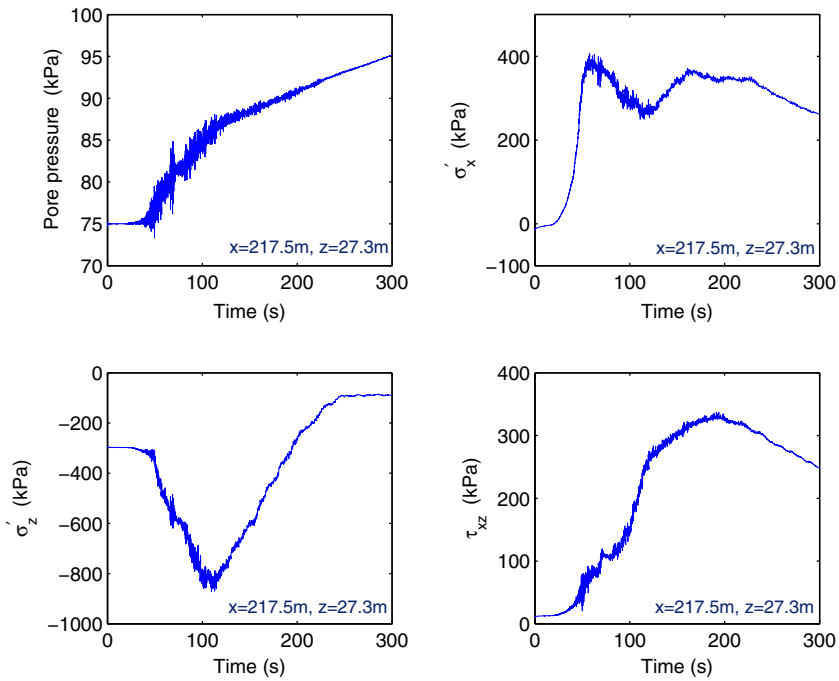

Fig. 5 Time history curve of pore pressure and effective stress in the rubble mound at position A ($x = 217.5$ m, $z = 27.3$ m)

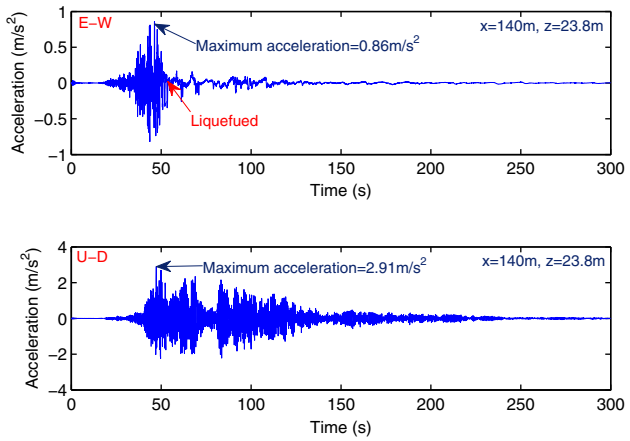

Fig. 6 Response acceleration time histories of the seabed foundation in EW and UD directions at position B ($x = 140$ m, $z = 23.8$ m)

soil cannot effectively transmit horizontal shear wave. On the other hand, the compressive wave (p-wave) in the U–D direction shows no obvious sign of abrupt change before and after liquefaction. Figure 7 illustrates this liquefaction process of seabed soil at position B. It is shown that the pore pressure quickly builds up once the seismic wave arrives at the computational domain; meanwhile, the effective stresses correspondingly decrease quickly. At time $t = 60$ s, the mean effective stress reaches a very small value (less than 1 kPa), and the pore pressure ratio becomes greater than 0.9, indicating the soil is close to liquefaction. On the other hand, the small effective stress in soil particles can still transmit shear waves between $t = 60$–200 s. As shown in Fig. 7, there is low amplitude E–W acceleration during that period. After $t = 200$ s, the E–W acceleration is almost zero, corresponding to zero mean effective stress in soils.

Figure 8a illustrates the horizontal displacement time histories at two typical positions C ($x = 50$ m, $z = 22$ m) and D ($x = 350$ m, $z = 29$ m), which are far away from the breakwater. It can be found that the far field sloping seabed is significantly displaced to the left up to 14–15 m. The lateral displacements at the two positions are similar before $t = 100$ s. After 100 s, the lateral displacement in the zone at the left-hand side of the breakwater becomes larger than that at the right-hand side. As discussed above, the breakwater begins to tilt and rotate after $t = 100$ s, which significantly affects the lateral spreading of the seabed soil at the right-hand side. The far-field seabed soil on the left-hand side freely moves to the left, whereas the lateral displacement of seabed soil at the right-hand side is constrained by the composite breakwater. This blockage effect by the composite breakwater can be also observed in Fig. 8b, which illustrates the vertical distribution of the lateral spreading along two cross sections at $t = 300$ s. The lateral spreading to the left along $x = 350$ m is much less than that along $x = 50$ m.

It can be observed from Fig. 8a that the lateral displacement to left side at the two typical positions (C and D) at the far-field seabed at $t = 100$ s is about 6 m; however, the horizontal displacement of the breakwater is only about 1 m at $t = 100$ s. This result indicates the distribution of lateral spreading in seabed foundation is not uniform due to

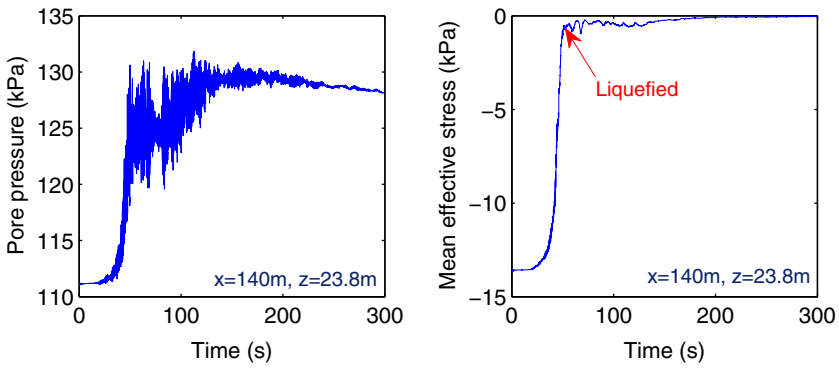

Fig. 7 Time history curve of pore pressure and effective stress in the seabed foundation at position B ($x = 140$ m, $z = 23.8$ m)

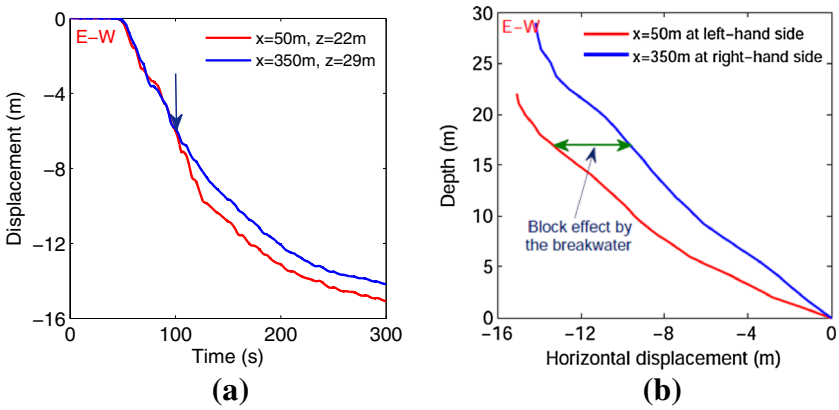

Fig. 8 Lateral spreading of the sloping seabed foundation at far field. **a** Horizontal displacement time histories at positions C ($x = 50$ m, $z = 22$ m) and D ($x = 350$ m, $z = 39$ m), **b** distribution of horizontal displacement along two cross sections at $t = 300$ s

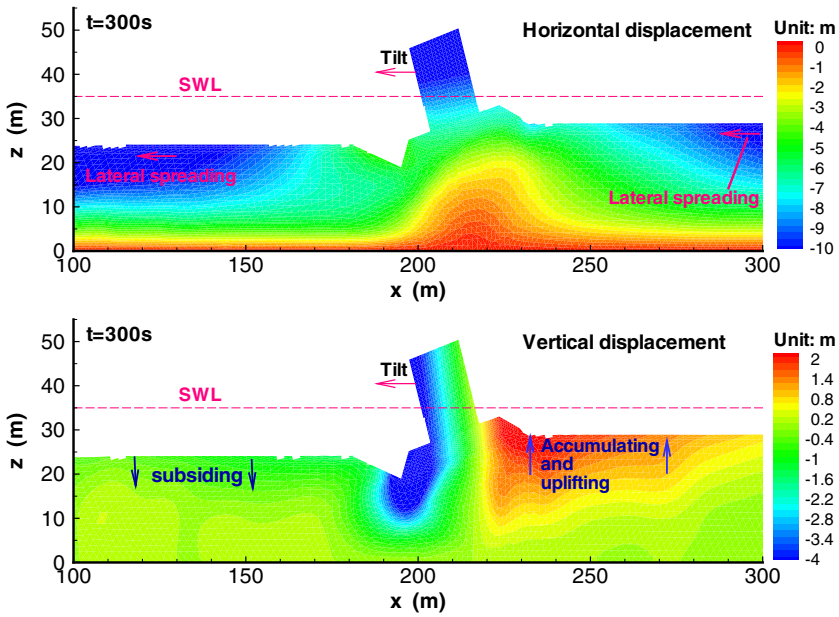

Fig. 9 Distribution of seismic wave-induced displacement in the seabed–composite breakwater system at $t = 300$ s

the presence of breakwater. The lateral spreading to the left of the seabed soil beneath and closed to the breakwater is much less than that of far-field seabed, as can be observed in Fig. 9. It can be also seen that there is a zone of seabed soil beneath the breakwater with virtually no lateral displacement. The displacement distribution indicates that weight of the breakwater can effectively constrain the movement of the seabed soil beneath and close to it.

The distribution of vertical displacement shown in Fig. 9b indicates that the seabed soil flowing from the far-

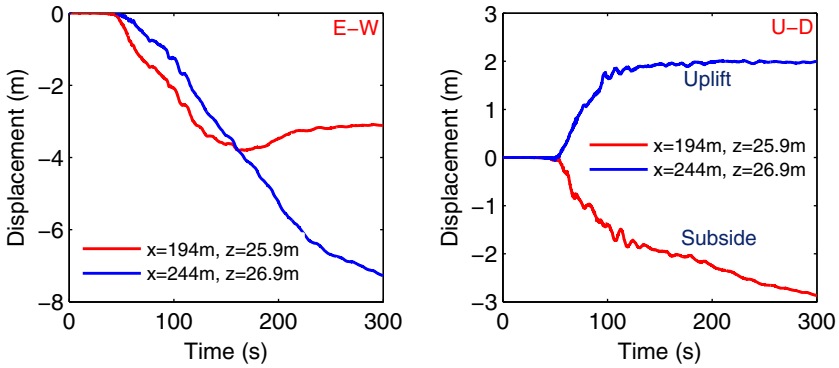

Fig. 10 Displacement time histories at near-field seabed foundation at position E ($x = 194$ m, $z = 25.9$ m) and position F ($x = 244$ m, $z = 26.9$ m)

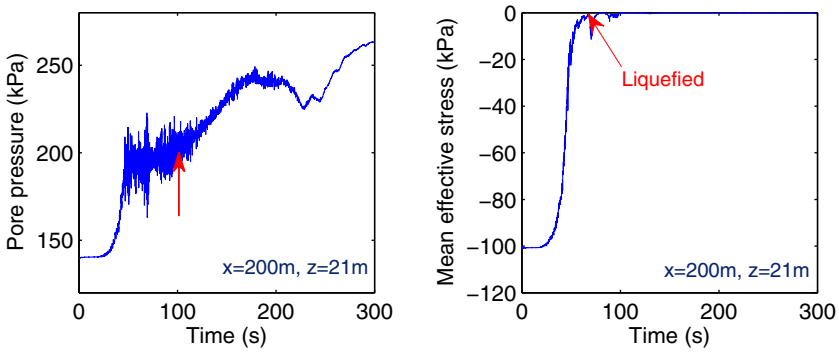

Fig. 11 Time history of pore pressure and effective stress in the seabed foundation at position G ($x = 200$ m, $z = 21$ m)

field at the right-hand side accumulates at the zone close to the breakwater due to the blockage effect of the breakwater mentioned above. As a result, the surface of the accumulation zone uplifts. On the other hand, the breakwater has no blockage effect on its left-hand side, and thus no accumulation zone exists in this region. To investigate the lateral displacement of the near-field seabed soil, another two positions, E ($x = 194$ m, $z = 25.9$ m) and F ($x = 244$ m, $z = 26.9$ m), are selected. Figure 10 illustrates the horizontal and vertical displacement time histories of these two positions. The horizontal displacements of E and F are 7 and 3 m to the left, respectively, which demonstrates again the blockage effect of the breakwater on the movement of near-field seabed soil. The vertical displacements of these two positions clearly show that the near-field seabed soil on the left-hand side subsides downward about 3 m in pace with the subsidence of the breakwater. The magnitude of uplifting of the near-field seabed soil on the right hand side is about 2 m. It is worth noting that the uplifting mainly occurs before $t = 100$ s. As the breakwater begins to tilt and rotate afterwards, the uplifting effect ceases. This phenomenon indicates that the movement of near-field seabed soil is closely related to the movement of the breakwater.

Apart from the acceleration and displacement responses, the seismic-induced variation of pore pressure and effective stress in the sloping seabed foundation are also important and need to be explored. Figure 11 illustrates the time history of pore pressure and mean effective stress at the position G ($x = 200$ m, $z = 21$ m) located under the left foot of the rubble mound. It can be observed that the pore pressure in the near-field builds up quickly under the seismic loading, as the mean effective stress decreases. The seabed soil becomes liquefied at $t = 60$ s since the mean effective stress approaches zero. It is worth mentioning that the pore pressure at the position G begins to increase again after $t = 100$ s. As mentioned above, the tilting and rotation of caisson shift the gravity center of the breakwater to the left side, causing sudden increase of overburden pressure. As a result, pore pressure at the position G ($x = 200$ m, $z = 21$ m) increases after $t = 100$ s in the partially drained compression process. This result indicates that the numerical model FSSI-CAS 2D is capable of capturing the nonlinear interaction between the breakwater and less dense seabed foundation.

Acceleration amplification spectrum

This section focuses on the acceleration amplification of the caisson. Three typical points are selected to demonstrate the characteristics of acceleration response spectrum of the breakwater-seabed system. They are located at the

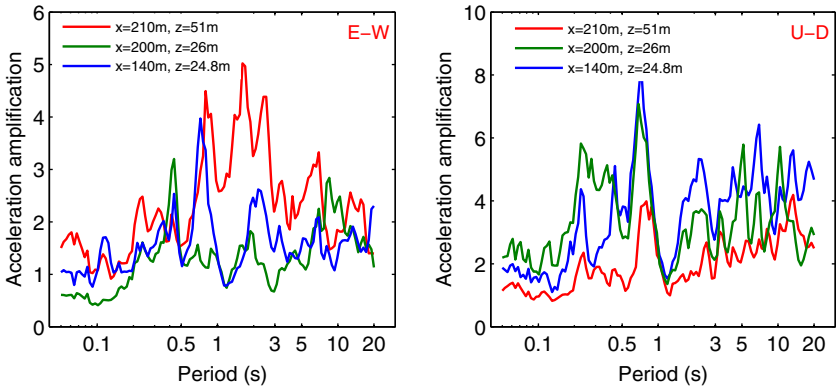

Fig. 12 Acceleration response amplification spectra at typical positions in the seabed–composite breakwater system

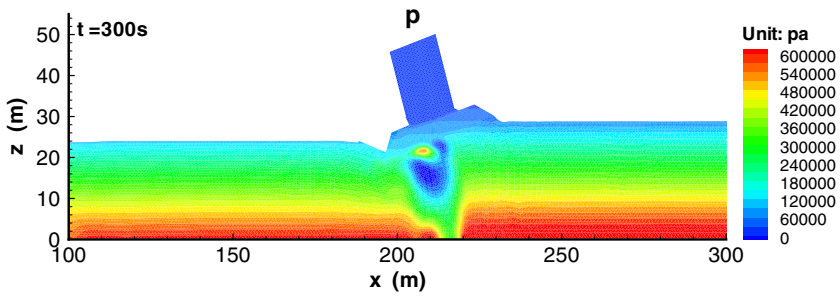

Fig. 13 Distribution of seismic wave-induced pore pressure in the seabed foundation

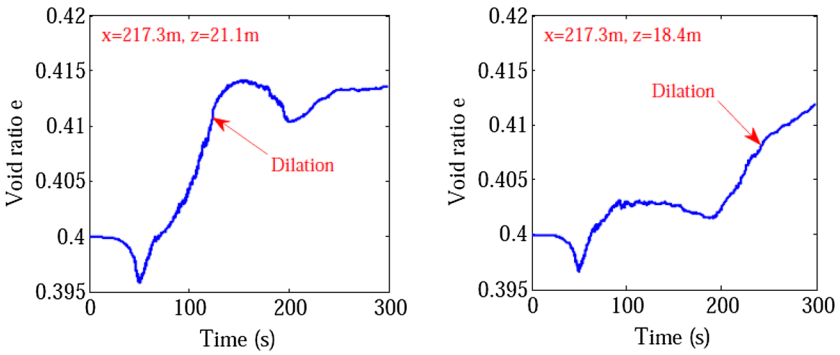

Fig. 14 Time history of void ratio e in the seabed foundation under the composite breakwater, showing dilation of the soil in lateral spreading after liquefaction

left-top corner of the caisson ($x = 210$ m, $z = 51$ m), left-bottom corner of the rubble mound ($x = 200$ m, $z = 26$ m), and a point at free field ($x = 140$ m, $z = 24.8$ m). Figure 12 illustrates the amplification spectrum for accelerations at these three positions. It can be observed that the amplification coefficients range from 0.5 to 5 in the E–W component, and from 1 to 8 in the U–D component. The maximum E–W amplification in the free field ($x = 140$ m $z = 24.8$ m) is achieved at the period of 0.7 s. The maximum E–W amplification at the left-bottom corner of the rubble mound is shortened to 0.4 s, maybe because the site is only partially liquefied. It is also interesting to find that the maximum amplification in the U–D component occurs at the period around 0.7 s.

Liquefaction of seabed foundation

Figure 13 displays the seismically induced pore pressure distribution at the end of shaking ($t = 300$ s). The pore pressure in the seabed floor at the right-hand side of the breakwater is slightly larger than that at the left-hand side, indicating that the rate of pore pressure buildup is greater at the right-hand side. On the other hand, the rate of pore water buildup in the seabed beneath the breakwater is apparently small. It is worth noting that a zero pore-pressure zone exists under the left part of the rubble mound, which is primarily due to the nonlinear interaction between the breakwater and its loose seabed foundation. As shown in Fig. 9, the horizontal displacement (4–6 m) of the

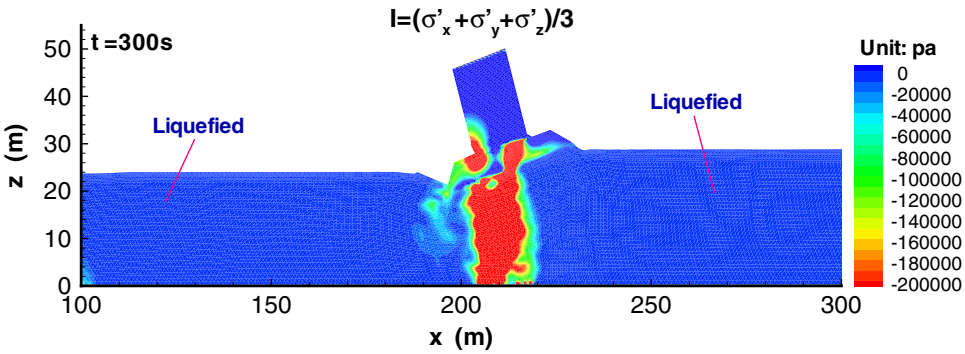

Fig. 15 Distribution of residual mean effective stress in the seabed foundation

seabed soil close to the left part of the rubble mound is greater than that in the zone under it (0–2 m). This movement mode causes dilation of the seabed soil underneath the rubble mound, and the void ratio becomes larger, as illustrated in Fig. 14. As a result, the pore water pressure in this zone decreases.

Figure 15 shows the distribution of mean effective stress at $t = 300$ s. It can be observed that the mean effective stress on the seabed foundation away from the breakwater is close to zero, where the seabed soil is fully liquefied under seismic loading. However, the mean effective stress underneath the breakwater is still greater than 200 kPa, indicating the seabed soil in this zone is only partially liquefied. The partially liquefied soil forms a load bearing column that prevented the breakwater from complete failure.

Conclusions

The offshore structures constructed on the sloping sediments in the offshore environment can subside, tilt, and rotate under seismic loading. Compared to very dense seabed soil, loose seabed soils can dampen more wave energy. The seismic resistance of offshore structures constructed on the loose or medium-dense seabed foundation is lower than those located on dense seabed foundation. Because of the seabed liquefaction, offshore structures on loose or medium-dense seabed foundation are prone to large lateral displacement, subsidence, and tilting. The computational results demonstrate that the shear wave cannot be transmitted in a liquefied seabed soil. The soil constitutive model PZIII is capable of capturing the post-liquefaction behaviors of soils.

There is intensive, complex, and nonlinear interaction between offshore structures and their seabed foundation. Although the seabed soil is completely liquefied after the strong shaking, overburden pressure due to the weight of offshore structures prevents complete liquefaction of the underlying seabed. The partially liquefied soil can still behave like a pile supporting its superstructure from a total failure.

Acknowledgments This study is supported by Hong Kong Research Grants Council (RGC) General Research Fund No. 16213615, RGC Collaborative Research Fund No. CityU8/CRF/13G, HKUST Post-Doctoral Fellowship Matching Fund, and National Natural Science Foundation of China under project No. 41472291. The authors also appreciate Professor Andrew Chan from Federation University Australia, who provided part of the computer code used in this study. Strong-motion data used in this study is obtained from KiK-net (http://www.kyoshin.bosai.go.jp/) operated by National Research Institute for Earth Science and Disaster Resilience (NIED) in Japan.

References

El Shamy U, Zeghal M, Dobry R, Thevanayagam S, Elgamal A, Abdoun T, Medina C, Bethapudi R, Bennett V (2010) Micromechanical aspects of liquefaction-induced lateral spreading. Int J Geomech 10(5):190–201

Elgamal A, Yang A, Lai T, Kutter BL, Wilson D (2005) Dynamic response of saturated dense sand in laminated centrifuge container. J Geotech Geoenviron Eng 131(5):598–609

Hsu TJ, Sakakiyama T, Liu PLF (2002) A numerical model for wave motions and turbulence flows in front of a composite breakwater. Coast Eng 46:25–50

Huang Y, Yashima A, Sawada K, Zhang F (2008) Numerical assessment of the seismic response of an earth embankment on liquefiable soils. Bull Eng Geol Environ 67(1):31–39

Lu J, Elgamal A, Yan L, Law K, Conte JP (2011) Large scale numerical modeling in geotechnical earthquake engineering. Int J Geomech 11(6):490–503

Manzanal D, Merodo JAF, Pastor M (2011) Generalized plasticity state parameter-based model for saturated and unsaturated soils. Part 1: saturated state. Int J Numer Anal Meth Geomech 35:1347–1362

Pastor M, Zienkiewicz OC, Chan AHC (1990) Generalized plasticity and the modelling of soil behaviour. Int J Numer Anal Meth Geomech 14:151–190

Pastor M, Chan AHC, Mira P, Manzanal D, Fernndez MJA, Blanc T (2011) Computational geomechanics: the heritage of olek zienkiewicz. Int J Numer Meth Eng 87(1–5):457–489

Sumer BM, Ansal A, Cetin KO, Damgaard J, Gunbak AR, Hansen NEO, Sawicki A, Synolakis CE, Yalciner AC, Yuksel Y, Zen K (2007) Earthquake-induced liquefaction around marine structures. J Waterway Port Coast Ocean Eng 133(1):55–82

Wang G, Sitar N (2011) Static and dynamic axial response of drilled piers II: numerical simulation. J Geotech Geoenviron Eng 137(12):1143–1153

Wang G, Xie Y (2014) Modified bounding surface hypoplasticity model for sands under cyclic loading. J Eng Mech 140(1):91–104

Xia ZF, Ye GL, HWang J, Ye B, Zhang F (2010) Fully coupled numerical analysis of repeated shake-consolidation process of earth embankment on liquefiable foundation. Soil Dyn Earthq Eng 30(11):1309–1318

Ye JH (2012a) Numerical analysis of wave-seabed-breakwater interactions. Ph.D thesis, Universtity of Dundee, Dundee, UK

Ye JH (2012b) Numerical modelling of consolidation of 2-D porous unsaturated seabed under a composite breakwater. Mechanika 18(4):373–379

Ye JH (2012c) Seismic response of poro-elastic seabed and compositebreakwater under strong earthquake loading. Bull Earthq Eng 10(4):1609–1633

Ye JH, Wang G (2015) Seismic dynamics of offshore breakwater on liquefiable seabed foundation. Soil Dyn Earthq Eng 76:86–99

Ye JH, Wang G (2016) Numerical simulation of the seismic liquefaction mechanism in an offshore loosely deposited seabed. Bull Eng Geol Environ (**in press**)

Ye B, Ye GL, Zhang F, Yashima A (2007) Experimental and numerical simulation of repeated liquefaction-consolidation of sand. Soils Found 3(47):547–558

Ye JH, Jeng D-S, Chan A (2012) Consolidation and dynamics of 3D unsaturated porous seabed under rigid caisson breakwater loaded by hydrostatic pressure and wave. Sci China Techn 55(8):2362–2376

Ye JH, Jeng D-S, Wang R, Zhu C (2013) Validation of a 2-d semi-coupled numerical model for fluid-structure-seabed interaction. J Fluid Struct 42:333–357

Zienkiewicz OC, Chang CT, Bettess P (1980) Drained, undrained, consolidating and dynamic behaviour assumptions in soils. Geotechnique 30(4):85–395

Zienkiewicz OC, Chan AHC, Pastor M, Schrefler BA, Shiomi T (1999) Computational geomechanics with special reference to earthquake engineering. Wiley, London